

1     **Overcoming chemical equilibrium limitations using a thermodynamically**  
2                                   **reversible chemical reactor**

3     Ian S. Metcalfe<sup>1\*</sup>, Brian Ray<sup>1</sup>, Catherine Dejoie<sup>2</sup>, Wenting Hu<sup>1</sup>, Chris de Leeuwe<sup>1</sup>, Cristina  
4     Dueso<sup>1</sup>, Francisco R. García-García<sup>3</sup>, Cheuk-Man Mak<sup>1</sup>, Evangelos I. Papaioannou<sup>1</sup>, Claire.  
5     R. Thompson<sup>1</sup> and John. S. O. Evans<sup>4</sup>

6     <sup>1</sup>School of Engineering, Newcastle University, Newcastle-upon-Tyne NE1 7RU, U.K.

7     <sup>2</sup>European Synchrotron Radiation Facility, 71 avenue des Martyrs, 38043 Grenoble, France

8     <sup>3</sup>School of Engineering, The University of Edinburgh, Edinburgh EH9 3FB, U.K.

9     <sup>4</sup>Department of Chemistry, Durham University, Durham DH1 3LE, U.K.

10

11    **All real processes be they chemical, mechanical or electrical, are thermodynamically**  
12    **irreversible and therefore suffer from thermodynamic losses. Here, we report the**  
13    **design and operation of a chemical reactor capable of approaching thermodynamically-**  
14    **reversible operation. The reactor was employed for hydrogen production via the water-**  
15    **gas shift reaction, an important route to ‘green’ hydrogen. The reactor avoids mixing**  
16    **reactant gases by transferring oxygen from the (oxidising) water stream to the**  
17    **(reducing) carbon monoxide stream via a solid-state oxygen reservoir consisting of a**  
18    **perovskite phase (La<sub>0.6</sub>Sr<sub>0.4</sub>FeO<sub>3-δ</sub>). This reservoir is able to remain close to equilibrium**  
19    **with the reacting gas streams because of its variable degree of non-stoichiometry and**  
20    **thus develops a ‘chemical memory’ which we employ to approach reversibility. We**  
21    **demonstrate this memory using operando, spatially-resolved, real-time, high-resolution**  
22    **x-ray powder diffraction on a working reactor. The design leads to a reactor**  
23    **unconstrained by overall chemical equilibrium limitations, which can produce**  
24    **essentially pure hydrogen and carbon dioxide as separate product streams.**

25

26 Reducing thermodynamic losses within the chemical industry has driven the design of highly  
27 efficient heat and mass transfer devices as well as the methodologies to enable such design<sup>1</sup>.  
28 However, the heart of any chemical process, the chemical transformation occurring within the  
29 reactor, has not yet received the same level of attention; there is currently no recipe for  
30 producing a thermodynamically reversible chemical reactor and most reactors manifest very  
31 significant irreversibilities<sup>2</sup>. Here we design and operate such a thermodynamically  
32 reversible reactor. One impact of the reactor is its ability to overcome overall reaction  
33 equilibrium limitations. This property is significant as many chemical reactions are  
34 reversible in nature and their conversions are limited by reaction equilibrium. Such  
35 limitations leads to incomplete conversion of reactants, which then exit the reactor mixed  
36 with the products. This results in enormous cost to the chemical industry which must design  
37 and operate complex separation schemes to purify products. Although Dudukovic<sup>3</sup> identifies  
38 combining reaction and separation as a key means of avoiding such equilibrium constraints,  
39 there have, until now, been no ways of avoiding equilibrium constraints without the need for  
40 a simultaneous separation.

41 Chemical transformations are conventionally performed via ‘mixed’ reactions.  
42 Multiple reactants, initially separate, are mixed, the reaction mixture is heated to the reaction  
43 temperature and the reaction is allowed to proceed. The very act of mixing results in  
44 significant thermodynamic losses (one will inevitably need to expend energy to separate the  
45 reactants and the individual products). It is, however, possible to avoid mixing using a  
46 dynamic approach often referred to as chemical looping<sup>4-7</sup>. Indeed some of the potential  
47 thermodynamic advantages of such an approach have been recognised for e.g. combustion  
48 processes<sup>8,9</sup>. There has, however, been no recognition of how a dynamic or ‘unmixed’  
49 approach could be used to overcome overall reaction equilibrium constraints.

50 Here we consider the reversible water-gas shift (WGS) reaction,

51



53

54 where  $\text{H}_2\text{O}$  is reacted with  $\text{CO}$  to produce  $\text{H}_2$  and  $\text{CO}_2$ . Reaction 1 is key to many  $\text{H}_2$   
55 production processes and performed on a very large scale industrially (total capacity of 50  
56 million tons per annum<sup>10</sup>). The reaction is equilibrium limited (Fig. 1a and Supplementary  
57 Video 1; a high-resolution version of the video can also be found at  
58 <http://nuvision.ncl.ac.uk/Play/18143>) and this leads to significant process complexity  
59 involving multiple reaction stages and separation. Overcoming this equilibrium limitation  
60 through the use of membranes<sup>11-13</sup> and  $\text{CO}_2$  absorption<sup>14-19</sup> has attracted considerable  
61 attention in the past. In a chemical-looping WGS reactor,  $\text{H}_2\text{O}$  (high oxidising potential) is  
62 first passed over a solid phase carrier of oxygen (oxygen carrier material or OCM) that  
63 accepts oxygen resulting in the production of  $\text{H}_2$ . Then in a second step  $\text{CO}$  (low oxidising  
64 potential) is passed over the solid phase, removing oxygen to produce  $\text{CO}_2$ .

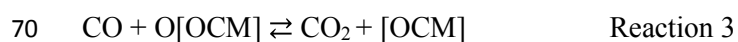
65

66 Step 1,  $\text{H}_2\text{O}$ -feed, bed-oxidation half cycle:



68

69 Step 2,  $\text{CO}$ -feed, bed-reduction half cycle:



71

72 Thus we avoid gas-phase mixing of the  $\text{H}_2\text{O}$  and  $\text{CO}$  reactants and exploit the fact that the  
73 WGS reaction is an oxygen transfer reaction by performing the transfer in two separate steps

74 (a H<sub>2</sub>O-feed, bed-oxidation half cycle and CO-feed, bed-reduction half cycle) through the use  
75 of an OCM. The conversion to products is then no longer limited by the chemical  
76 equilibrium of Reaction 1 but rather by the individual equilibria associated with Reactions 2  
77 and 3. Conventional OCMs, such as metal-metal oxides, function by donating oxygen and  
78 receiving oxygen, at the fixed oxygen chemical potentials associated with their phase  
79 transitions (Fig. 1b). The practical consequence of this is that one can never have an OCM  
80 that gives a high conversion for both Reaction 2 and Reaction 3 at the same time (Fig. 1c and  
81 1d). The chemical-looping reactor's operation is also compromised thermodynamically  
82 because the driving force for oxygen exchange between gas and solid can never be  
83 vanishingly small. This is because the oxygen resides in the solid at a fixed oxygen chemical  
84 potential, whereas in the gas phase, there is a variable oxygen chemical potential as the gas  
85 composition must, for any reasonable conversion, change significantly between reactor inlet  
86 and outlet. In fact by some measures such a reactor can perform no better than a  
87 conventional 'mixed' reactor (Supplementary Video 1 and Supplementary Information  
88 Section 2).

89 An alternative way of viewing the process is that the OCM is required to transfer  
90 chemical information between the H<sub>2</sub>O-feed half cycle and CO-feed half cycle for the reactor  
91 to operate. A conventional metal-metal oxide system involving a single phase transition  
92 (between metal and metal oxide) stores no information about the oxygen chemical potential  
93 of the gases to which it has been exposed other than they were sufficiently reducing or  
94 oxidising to cause the phase transition. So a single OCM does not have the chemical memory  
95 to transfer sufficient information (i.e., the full oxidising and reducing potential of feed gases)  
96 for the reactor to achieve high conversions in both half cycles. In theory, it would be possible  
97 to transfer more information between half cycles by using axially-separated OCMs with  
98 differing oxygen chemical potentials associated with their phase transitions and moving to a

99 reverse flow design (oxidising and reducing feeds are fed to opposite end of the reactor). The  
100 OCMs would need to be spatially arranged such that the most easily oxidised is at the end of  
101 the bed which is exposed to the oxidising feed and the most easily reduced at the reducing  
102 feed end. We show in the Supplementary Information that, for the WGS reaction at 820°C, if  
103  $n$  phase transitions are available using a series of  $n$  conventional OCM materials, a maximum  
104 conversion of  $n/(n+1)$  can be achieved (Supplementary Information Section 2).  
105 Unfortunately, this approach, whilst an improvement, would require large numbers of  
106 different OCMs to achieve high conversions and would be inflexible if the redox ability of  
107 feeds and/or products were changed. If two phase transitions were available within a single  
108 material a further benefit can be gained<sup>20</sup> but the system would still lack the flexibility to  
109 respond to changing inlet redox abilities (full discussion in Supplementary Information  
110 Section 2).

111 Here we demonstrate that a ‘chemical memory reactor’ can be built using a single  
112 OCM capable of transferring the necessary information for thermodynamically reversible  
113 operation between the two half cycles. The OCM can only perform this function in the  
114 absence of mixing in the solid phase in order to allow spatially-resolved information to be  
115 stored, transferred between half cycles and subsequently read. The oxidising end of the bed  
116 must remember the oxygen chemical potential of the most oxidising gas it experiences and  
117 the reducing end must remember the oxygen chemical potential of the most reducing gas it  
118 experiences throughout the cycles. We therefore need an oxygen carrier that can support the  
119 full range of oxygen chemical potentials required (Figure 1e and 1f). This leads us to select  
120 an oxide of variable oxygen non-stoichiometry as OCM<sup>21,22</sup>, such OCMs having been used  
121 previously in chemical looping for kinetic or stability benefits<sup>23,24</sup>. In these materials we  
122 know that the oxygen content will be a continuous function of oxygen chemical potential  
123 (furthermore we employ oxidising and reducing streams that can exhibit defined oxygen

124 chemical potentials, here achieved by the presence of two distinct redox couples,  $H_2/H_2O$  and  
125  $CO_2/CO$ ). To summarise, in order to transfer the chemical information required between half  
126 cycles, we must simultaneously use reverse flow (so that one end of the bed is always  
127 oxidised and the other always reduced), we must use a solid that can support the full range of  
128 oxygen chemical potentials required (so that its state can reflect that of the reactant streams)  
129 and we must use a solid phase held within a fixed bed (so that solid phase mixing does not  
130 result in loss of chemical information).

131 Our 'chemical memory reactor' then consists of a bed of a non-stoichiometric oxide  
132 OCM operated in reverse gas flow (Fig. 1e and 1f) which permits an extensive exchange of  
133 chemical information through the OCM between each half cycle. Repeated application of the  
134 oxidising feed to the oxidising end of the bed and the reducing feed to the reducing end of the  
135 bed causes an oxidation state profile to develop along the length of the bed (Fig. 1g and 1h  
136 and Supplementary Video 1). Provided each half cycle is short enough that we do not  
137 destroy this oxidation state profile ('memory'), the bed will 'remember' the oxygen chemical  
138 potentials associated with its feed streams. The gradual oxidation state profile also leads to  
139 small thermodynamic driving forces for the reactions occurring at each point along the  
140 reactor's length and it therefore approaches reversible operation. Whilst recognizing the  
141 constraint that the reducing product stream can be no more reducing than the reducing feed  
142 and the oxidising product stream no more oxidising than the oxidising feed, we may achieve  
143 arbitrarily high overall conversion of the individual Reactions 2 and 3 and hence the overall  
144 Reaction 1.

145

146 **Results**

147 To prove both the concept and the mechanism, an unmixed water-gas shift reaction was  
148 performed in such a reverse-flow memory reactor with a non-stoichiometric LSF  
149 ( $\text{La}_{0.6}\text{Sr}_{0.4}\text{FeO}_{3-\delta}$ ) perovskite oxygen-carrier material (Supplementary Information Section 1).  
150 The nominal temperature of operation ( $820^\circ\text{C}$ ) was chosen such that the equilibrium constant  
151 for the conventional mixed water-gas shift reaction (Reaction 1),  $K$ , is unity (the measured  
152 temperature in the reactor ranges from  $790^\circ\text{C}$  to  $820^\circ\text{C}$  causing the equilibrium constant to  
153 vary between 1.12 and 1.01).  $\text{La}_{0.6}\text{Sr}_{0.4}\text{FeO}_{3-\delta}$  was judged to be appropriate for use at this  
154 temperature as it is known to be both oxygen non-stoichiometric and stable over a very large  
155 range of oxygen chemical potentials, and remains single phase throughout the temperature  
156 and oxygen partial pressure range of our experiments. At the temperature of operation,  
157 oxygen capacity comes from reduction of Fe(III) to Fe(II) accompanied by oxygen vacancy  
158 formation. Oxygen is able to rapidly enter and leave the OCM structure as a result of both  
159 high oxygen-ion and electron conductivity.

160 The reactor was housed in a custom-made furnace and operated at the high-resolution  
161 x-ray powder diffraction beam line (ID22) of the European Synchrotron Radiation Facility  
162 (ESRF). As an indicator that equilibrium has been overcome, we evaluate for each cycle a  
163 variable,  $K^*$  (Supplementary Information Section 2), which measures the reactor performance  
164 and is maximised for simultaneously high conversions to both  $\text{H}_2$  and  $\text{CO}_2$ ,

165

$$166 \quad K^* = \frac{\bar{y}_{\text{H}_2}\bar{y}_{\text{CO}_2}}{\bar{y}_{\text{H}_2\text{O}}\bar{y}_{\text{CO}}} \quad \text{Equation 1}$$

167

168 where  $\bar{y}_i$  is a time-averaged mole fraction at the reactor outlet. For a conventional mixed-  
169 reactant reactor,  $K^*$  would never be able to exceed the water-gas-shift equilibrium constant,  
170  $K$ , of unity. Practically this means that conversions to  $\text{H}_2$  and  $\text{CO}_2$  would not be able to

171 exceed 50% for a stoichiometric feed. Similarly, the  $n/(n+1)$  conversion limitation discussed  
172 above means that  $K^*$  can never exceed unity for an oxygen-carrier material with a single  
173 phase-transition such as that in Fig. 1c and 1d. Our non-stoichiometric oxide, however,  
174 behaves as if it supplies a very large number of phase transitions and thus there is no upper  
175 limit to the value of  $K^*$ . Experimentally, we observe  $K^*$  values much greater than unity  
176 when we operate our reactor as shown in Fig. 2a. As the bed used was prepared in an  
177 oxidised state, initial high conversions of CO to CO<sub>2</sub> are achieved with lower conversions of  
178 H<sub>2</sub>O to H<sub>2</sub> (Region A of Fig. 2a and Supplementary Fig. 7). After cycling, a profile of  
179 oxidation state of the material becomes established and each cycle becomes repeatable with  
180 conversions of H<sub>2</sub>O and CO equal within uncertainty (as the amount of oxidation in a H<sub>2</sub>O-  
181 feed half cycle must equal the reduction in a CO-feed half cycle), and both in excess of 75%;  
182  $K^*$  is observed to have a value of approximately 14 (Region B of Fig. 2a, Fig. 2b and  
183 Supplementary Fig. 7). It is quite clear that equilibrium limitations ( $K^* = 1$ ) have been  
184 overcome. Furthermore, the behaviour of the reactor was modelled by assuming plug-flow in  
185 the gas phase and gas-solid equilibrium with no adjustable parameters (Supplementary  
186 Information Section 7). Fig. 2e shows the outlet mole fractions versus time from the model.  
187 Good agreement is seen with Fig. 2b and similar conversions and value of  $K^*$  are predicted.  
188 By simple valve switching our reactor produces the pure, separated H<sub>2</sub> and CO<sub>2</sub> products of  
189 Reaction 1 from different ends of the bed.

190 Spatially- and temporally-resolved powder x-ray diffraction was used to investigate the state  
191 of the LSF oxygen-carrier material during reactor operation (there was no evidence for the  
192 formation of any additional phases during operation). Shifts in  $2\theta$  peak positions (Fig. 3a,  
193 Supplementary Fig. 3 and more discussion in Supplementary Information Section 4) were  
194 used to determine changes in lattice parameter which, with calculated chemical and thermal  
195 expansion coefficients and a defect chemistry model (Supplementary Information Section 1),



196 were used to calculate the oxygen content of the material as a function of position in the bed  
197 immediately after oxidation and reduction half cycles (Fig. 3b). It is evident that a profile in  
198 the oxidation state of the non-stoichiometric material has developed as predicted.  
199 Furthermore, although the degree of oxidation of the OCM increases after bed oxidation at  
200 every location investigated in the bed compared to immediately after bed reduction, it is clear  
201 that the bed retains an oxidation state profile throughout.

202 To test the concept of chemical memory further we predict that we can improve the  
203 memory of the bed and improve conversions by shortening the half-cycle durations (less  
204 oxygen is removed and added in each cycle). Thus we see in Fig. 2c, that when the half-  
205 cycle duration is reduced from 60 seconds to 48 seconds both conversions increase from in  
206 excess of 75% to in excess of 80%, and  $K^*$  doubles from 14 to 28. When the duration  
207 increases, Fig. 2d, we expect a loss of memory and we see that a 120-second duration results  
208 in a decrease of conversions to barely more than 50%;  $K^*$  decreases to 1.4. This dependence  
209 of  $K^*$  on half-cycle duration is also confirmed by use of the thermodynamic model of the  
210 reactor (Fig. 2e, Fig. 2f, Fig. 2g). The model predicts values of  $K^*$  in Regions B, C and D of  
211 13, 41 and 1.35 compared to the experimentally obtained values of 14, 28 and 1.4. Thus it  
212 appears that the reactor does not suffer from significant kinetic limitations. Furthermore, we  
213 may use a reactor bed with a fully developed oxidation state profile for the reverse water-gas  
214 shift reaction (Supplementary Fig. 9). By feeding  $H_2$  to the reduced end of the bed and  $CO_2$   
215 to the oxidised end we instantly achieve conversions in excess of equilibrium limitations.  
216 Such facile switching between forward and reverse reactions is unique to a reversibly-  
217 operated chemical memory reactor.

218

219 **Discussion**

220 The hydrogen produced by the reactor is free of carbon monoxide as no carbon is carried over  
221 from the reduction cycle to the hydrogen production cycle. This addresses a key challenge in  
222 hydrogen production. Furthermore, because of a lack of equilibrium limitations, the  
223 exothermic reaction can be performed at high temperature (taking a high temperature feed  
224 from a reforming or gasification process) and thus capitalise on the high kinetic rates  
225 available, even in the absence of a shift catalyst. So, whereas conventional hydrogen  
226 production requires two reactors (a high and a low temperature shift reactor) to drop carbon  
227 monoxide mole fractions to reasonable levels and then a separation step to remove carbon  
228 dioxide from the hydrogen, our reactor accomplishes all of these steps in one unit and has  
229 kinetics that are more favourable than a conventional process. This, if applied practically,  
230 could lead to significantly reduced hydrogen-production process footprints and costs. We  
231 must also note that the OCM is stable over a larger number of cycles. 300 cycles were  
232 performed with no measurable deterioration in  $K^*$  (Supplementary Fig. 7) or change in OCM  
233 morphology (Supplementary Fig. 8). The origin of the OCM stability presumably results  
234 from the ability of the OCM to donate and receive oxygen without a phase change.

235         It may be possible to implement more complex reaction schemes involving the  
236 introduction of methane (or natural gas) as the reducing feed. Internal reforming of the  
237 methane with lattice oxygen from the OCM would result in syngas formation. It would be  
238 possible to operate such a reactor in a number of modes optimised for e.g. combined syngas  
239 and hydrogen production or hydrogen production alone. Depending on the application area  
240 more than two feeds could be desirable with the use of, e.g., an air feed to ensure an overall  
241 autothermal process if reforming a hydrocarbon feed. This raises the possibility of using  
242 single reactors, albeit dynamically operated, for the conversion of natural gas to hydrogen.

243         It must be noted that the ‘memory reactor’ concept developed here does not only  
244 apply to oxygen exchange reactions. Materials with non-stoichiometry in, e.g., hydrogen also

245 exist. It may be possible to apply such materials to reversibly couple hydrogenation and  
246 dehydrogenation reactions. This application could be crucial if chemical hydrogen storage  
247 becomes more important as one would be able to regenerate hydrogen at its supply pressure  
248 without significant energy input.

249

## 250 **Methods**

### 251 **Material synthesis**

252  $\text{La}_{0.6}\text{Sr}_{0.4}\text{FeO}_3$  was synthesised via the sol-gel method using stoichiometric ratios of  
253  $\text{Fe}(\text{NO}_3)_3(\text{H}_2\text{O})_9$  (Sigma Aldrich 216828),  $\text{La}(\text{NO}_3)_3(\text{H}_2\text{O})_6$  (Sigma Aldrich 61520), and  
254  $\text{Sr}(\text{NO}_3)_2$  (Sigma Aldrich 243426) mixed with citric acid (Sigma Aldrich 791725) and  
255 ethylene glycol (Sigma Aldrich 324558) in molar ratios to the total cations present of 1:1 and  
256 1.2:1 respectively. The total cation quantity was chosen to make 100 g of  $\text{La}_{0.6}\text{Sr}_{0.4}\text{FeO}_3$ . 450  
257 mL of deionised  $\text{H}_2\text{O}$  was added and the solution was stirred, decanted into a 10 L beaker and  
258 dried at  $60^\circ\text{C}$  for 48 hours. The resulting orange cake was lightly crushed and placed in a  
259 covered 700 mL alumina high form crucible and heated to  $1050^\circ\text{C}$  at  $1^\circ\text{C min}^{-1}$  and held for  
260 18 hours. The resulting powder was then sieved to select particle sizes between 80 and 160  
261  $\mu\text{m}$ .

262

### 263 **Flow system and reference experiments**

264 The flow system (Supplementary Fig. 2) employed 4-way cross-over valves to switch the gas  
265 composition being fed to the fixed-bed reactor, switch direction of feed to the reactor and to  
266 maintain continuous flow through the reactor and the gas analysis equipment. One complete  
267 redox cycle contained six phases, two phases of reactive gas feed of CO or  $\text{H}_2\text{O}$  and four

268 phases with an inert (argon) feed. The directional change of the feed to the reactor was  
269 always performed during an inert feed.

270 The system was operated with a furnace set point of 820°C in a vertical orientation for  
271 the *operando* x-ray diffraction studies on ID22 at ESRF and in a horizontal orientation for a  
272 long-term stability experiment (Supplementary Fig. 7), the reverse WGS experiment  
273 (Supplementary Fig. 9) and two further reference experiments involving a conventional  
274 mixed-reactant WGS experiment and an empty reactor with unmixed reactants  
275 (Supplementary Fig. 10). All total flows were set (unless otherwise stated) to  $3.4 \times 10^{-5} \text{ mol s}^{-1}$   
276 ( $50 \text{ ml min}^{-1}$  at NTP).

277

### 278 ***Operando* XRD setup**

279 The *operando* XRD reactor bed was held in a vertical furnace at a nominal 820°C and  
280 consisted of LSF641 powder, 1.43 g ( $6.43 \times 10^{-3} \text{ mol}$ ), packed into a quartz tube with an  
281 internal diameter of 4 mm with 2 mm wall thickness to form a fixed-bed reactor that was  
282 114.5 mm long. Local temperature was recorded with a K-type thermocouple placed in  
283 contact with the reactor tube which was allowed to equilibrate over 10 minutes. The local  
284 temperature was found to be 790°C at the bottom of the reactor bed, 810°C in the middle and  
285 820°C at the top. This leads to a thermally-induced variation of oxygen content in the  
286 absence of reaction which is accounted for in our analysis.

287 *Operando* X-ray powder diffraction was conducted at the high-resolution powder  
288 diffraction beamline ID22 at ESRF (MA2914) using the multi-analyser stage<sup>25</sup>. The energy  
289 used was 38 keV. The multi-analyser stage is composed of nine Si 111 analyser crystals  
290 preceding nine scintillator detectors, the detector channels being 2 degrees apart. The  $2\theta$  arm  
291 was scanned from 9 to 11.2 degrees ( $2\theta$ ) at a speed of  $4 \text{ degrees min}^{-1}$ . This setup yielded a

292 total effective scan range of 1 to 19.2 degrees, binned to 0.002 degree resolution, with 0.2  
293 degree overlap between each detector. The effective scan time was 36 seconds when  
294 initialisation of the positioner at the beginning of each scan was taken into account.

295

#### 296 **Data availability statement**

297 Data supporting this publication is openly available under an “Open Data Commons Open  
298 Database License”. The data with additional metadata are available at  
299 <http://dx.doi.org/10.17634/080913-1>

300

#### 301 **References**

- 302 1. Dincer, I., Cengel Y. A. Energy, entropy and exergy concepts and their roles in thermal  
303 engineering. *Entropy* **3**(3), 116-149 (2001).
- 304 2. Dunbar W. R., Lior N. Sources of combustion irreversibility. *Combust. Sci. Technol.* **103**,  
305 41-61 (1994).
- 306 3. Dudukovic M. P. Frontiers in Reaction Engineering. *Science* **325**, 698-701 (2009).
- 307 4. Thursfield A., Murugan A., Franca R., Metcalfe I. S. Chemical looping and oxygen  
308 permeable ceramic membranes for hydrogen production-a review. *Energy & Environ. Sci.*  
309 **5**, 7421-7459 (2012).
- 310 5. Adanez J., Abad A., Garcia-Labiano F., Gayan P., de Diego L. F. Progress in chemical-  
311 looping combustion and reforming technologies. *Prog. Energy Combust. Sci.* **38**, 215-282  
312 (2012).
- 313 6. Fan L.S., *Chemical looping systems for fossil energy conversions*. (Wiley-AIChE,  
314 Hoboken, NJ, 2010), pp. 241-249.
- 315 7. Lyngfält A., Leckner B., Mattisson T. A fluidised-bed combustion process with inherent  
316 CO<sub>2</sub> separation; application of chemical-looping combustion. *Chem. Eng. Sci.* **56**(10),  
317 3101-3113 (2001).
- 318 8. Richter H. J., Knoche K. F. Reversibility of Combustion Processes. *Acs Sym Ser* **235**, 71-  
319 85 (1983).
- 320 9. Anhedena M., Svedberga G. Exergy analysis of chemical-looping combustion systems.  
321 *Eng. Convers. Manag.* **39**, 1967-1980 (1998).
- 322 10. U.S. Department of Energy Hydrogen and Fuel Cell Technical Advisory Committee,  
323 “Report of the Hydrogen Production Expert Panel” (2013);  
324 [www.hydrogen.energy.gov/pdfs/hpep\\_report\\_2013.pdf](http://www.hydrogen.energy.gov/pdfs/hpep_report_2013.pdf).
- 325 11. Lu G. Q., da Costa J. C. D., Duke M., Giessler S., Socolow R., Williams R. H., Kreutz T.  
326 Inorganic membranes for hydrogen production and purification: A critical review and  
327 perspective. *J. Colloid Interface Sci.* **314**, 589-603 (2007).
- 328 12. Giessler S., Jordan L., da Costa J. C. D., Lu G. Q. Performance of hydrophobic and  
329 hydrophilic silica membrane reactors for the water gas shift reaction. *Sep. Purif. Technol.*  
330 **32**, 255-264 (2003).

- 331 13. Basile A., Criscuoli A., Santella F., Drioli E. Membrane reactor for water gas shift  
332 reaction. *Gas Sep. Purif.* **10**, 243-254 (1996).
- 333 14. Noor T., Gil M. V., Chen D. Production of fuel-cell grade hydrogen by sorption enhanced  
334 water gas shift reaction using Pd/Ni-Co catalysts. *Appl. Catal., B* **150**, 585-595 (2014).
- 335 15. Jang H. M., Kang W. R., Lee K. B. Sorption-enhanced water gas shift reaction using  
336 multi-section column for high-purity hydrogen production. *Int. J. Hydrogen Energy* **38**,  
337 6065-6071 (2013).
- 338 16. Jang H. M., Lee K. B., Caram H. S., Sircar S. High-purity hydrogen production through  
339 sorption enhanced water gas shift reaction using K<sub>2</sub>CO<sub>3</sub>-promoted hydrotalcite. *Chem.*  
340 *Eng. Sci.* **73**, 431-438 (2012).
- 341 17. Harrison D. P. Sorption-enhanced hydrogen production: A review. *Ind. Eng. Chem. Res.*  
342 **47**, 6486-6501 (2008).
- 343 18. Ortiz A. L., Harrison D. P. Hydrogen production using sorption-enhanced reaction. *Ind.*  
344 *Eng. Chem. Res.* **40**, 5102-5109 (2001).
- 345 19. Balasubramanian B., Ortiz A. L., Kaytakoglu S., Harrison D. P. Hydrogen from methane  
346 in a single-step process. *Chem. Eng. Sci.* **54**, 3543-3552 (1999).
- 347 20. Kathe M. V., Empfield A., Na J., Blair E., Fan L-S. Hydrogen production from natural  
348 gas using an iron-based chemical looping technology: Thermodynamic simulations and  
349 process system analysis. *Appl. Energy* **165**, 183-201 (2016).
- 350 21. Mizusaki J., Yoshihiro M., Yamauchi S., Fueki K. Nonstoichiometry and defect structure  
351 of the perovskite-type oxides La<sub>1-x</sub>Sr<sub>x</sub>FeO<sub>3-δ</sub>. *J. Solid State Chem.* **58**, 257-266 (1985).
- 352 22. Sogaard M., Hendriksen P. V., Mogensen M. Oxygen nonstoichiometry and transport  
353 properties of strontium substituted lanthanum ferrite. *J. Solid State Chem.* **180**, 1489-1503  
354 (2007).
- 355 23. Rydén M., Lyngfelt A., Mattisson T., Chen D., Holmen A., Bjørgum E. Novel oxygen-  
356 carrier materials for chemical-looping combustion and chemical-looping reforming;  
357 La<sub>x</sub>Sr<sub>1-x</sub>Fe<sub>y</sub>Co<sub>1-y</sub>O<sub>3-δ</sub> perovskites and mixed-metal oxides of NiO, Fe<sub>2</sub>O<sub>3</sub> and Mn<sub>3</sub>O<sub>4</sub>. *Int.*  
358 *J. Hydrog. Energy* **2**, 21-36 (2008).
- 359 24. Murugan A., Thursfield A., Metcalfe I. S. A chemical looping process for hydrogen  
360 production using iron-containing perovskites. *Energy Environ. Sci.* **4**, 4639-4649 (2011).
- 361 25. Hodeau J-L., P. Bordet, Anne M., Prat A., Fitch A. N., Dooryhee E., Vaughan G., Freund  
362 A. K. Nine-crystal multi-analyser stage for high resolution powder diffraction between 6  
363 and 40 keV. *SPIE Proceedings* **3348**, 353-361 (1998).

364

### 365 Acknowledgments

366 CT, CdL thank EPSRC for funding via a doctoral training award. The research leading to  
367 these results has received funding from the European Research Council under the European  
368 Union's Seventh Framework Programme (FP/2007-2013) / ERC Grant Agreement Number  
369 320725 and from the EPSRC via grants EP/G012865/1, EP/J016454/1 and EP/K029649/1,  
370 EP/P007767/1, EP/P024807/1. We thank Andy Fitch, Carlotta Giacobbe, Mauro Coduri and  
371 Olivier Grimaldi at ESRF for help with XRD and Trevor Ingham, IGI Systems Ltd., for  
372 constructing the custom flow system and furnace. We thank Alan Coelho for developments  
373 in Topas to enable analysis of the multiple x-ray data sets produced. We thank Dr Brad  
374 Ladewig with help in producing the video.

375

### 376 **Author contributions**

377 ISM conceived the overall idea, secured funding, and managed the work. ISM, JSOE wrote  
378 the main text. ISM, BR, WH, CdL, JSOE were responsible for the data analysis, modelling  
379 and interpretation. BR, CD, CdL, CD, FGG, CM, EIP, CRT, performed the experiments.

380

### 381 **Competing interests**

382 The authors declare no competing interests.

383

### 384 **Additional information**

385 Supplementary Information is linked to the online version of the paper at  
386 [www.nature.com/nchem/](http://www.nature.com/nchem/).

387

388 **Reprints and permissions information** is available at [www.nature.com/reprints](http://www.nature.com/reprints)

389

390 **Correspondence and requests for materials** should be addressed to  
391 [ian.metcalfe@newcastle.ac.uk](mailto:ian.metcalfe@newcastle.ac.uk).

392

### 393 **List of figure captions**

394 **Fig. 1. Thermodynamic reversibility in a water-gas shift reactor.** Colour coding of  
395 oxygen chemical potentials in the gas phase and oxygen content in the solid phase (red to  
396 blue for oxidising to reducing) is used to show that within conventional mixed gas reactors  
397 and metal-metal oxide chemical looping reactors the reactants cannot be fully converted. **(a)**  
398 Conventional WGS reactor producing a mixture of reactants and products. **(b)** Equilibrium  
399 relationship for a metal-metal oxide showing solid-phase oxygen content versus oxygen  
400 chemical potential of the gas phase. Note that only orange and light blue potentials are  
401 required to show where the phase transition lies. **(c)** The use of such a metal-metal oxide  
402 OCM for H<sub>2</sub> production in a chemical looping cycle where water is fed over the metal. The  
403 phase transition is not sufficiently reducing to produce a high mole fraction of H<sub>2</sub>. **(d)**  
404 Reduction of the metal oxide (CO is fed from the opposite end of the bed to H<sub>2</sub>O) cannot  
405 produce a high mole fraction of CO<sub>2</sub>. **(e)** The mode of operation of our memory reactor. The  
406 reactor contains a non-stoichiometric oxygen carrier (e.g. a perovskite, ABO<sub>3-δ</sub>) and operates  
407 under reverse flow with feeds of 5% CO (during the reduction step) and 5% H<sub>2</sub>O (during the  
408 oxidation step). The reactive stages are preceded and followed by a flow of argon. **(f)**  
409 Equilibrium relationship for a non-stoichiometric oxide showing solid-phase oxygen content  
410 versus gas phase oxygen chemical potential. Note that oxygen capacity is available over the  
411 entire range of oxygen chemical potentials. **(g and h)** A non-stoichiometric oxide develops a  
412 profile of oxidation states along the bed allowing the production of pure products if cycle  
413 durations do not remove the profile from the bed. **(g)** A H<sub>2</sub>O feed is converted almost  
414 entirely to H<sub>2</sub> as the H<sub>2</sub> exits over the reduced end of the bed before **(h)** switching the  
415 direction of flow and converting CO almost entirely to CO<sub>2</sub> as the CO<sub>2</sub> exits over the oxidised  
416 end of the bed. More explanation of the reactor concept can be found elsewhere  
417 (Supplementary Video 1).

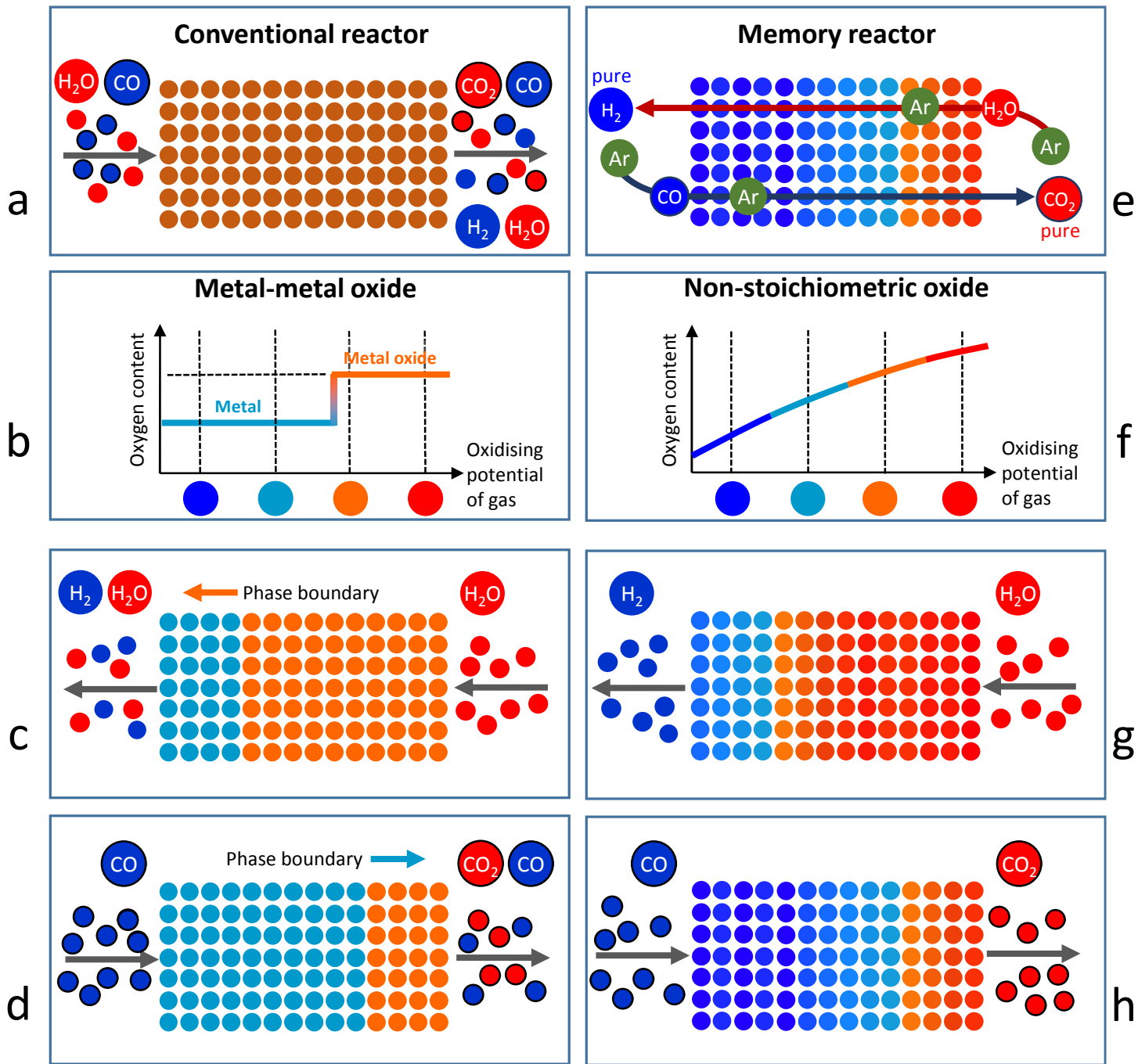
418

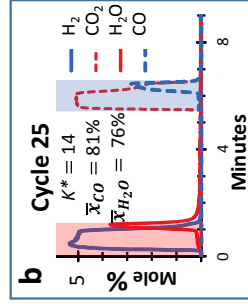
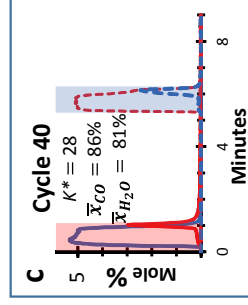
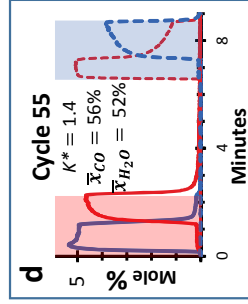
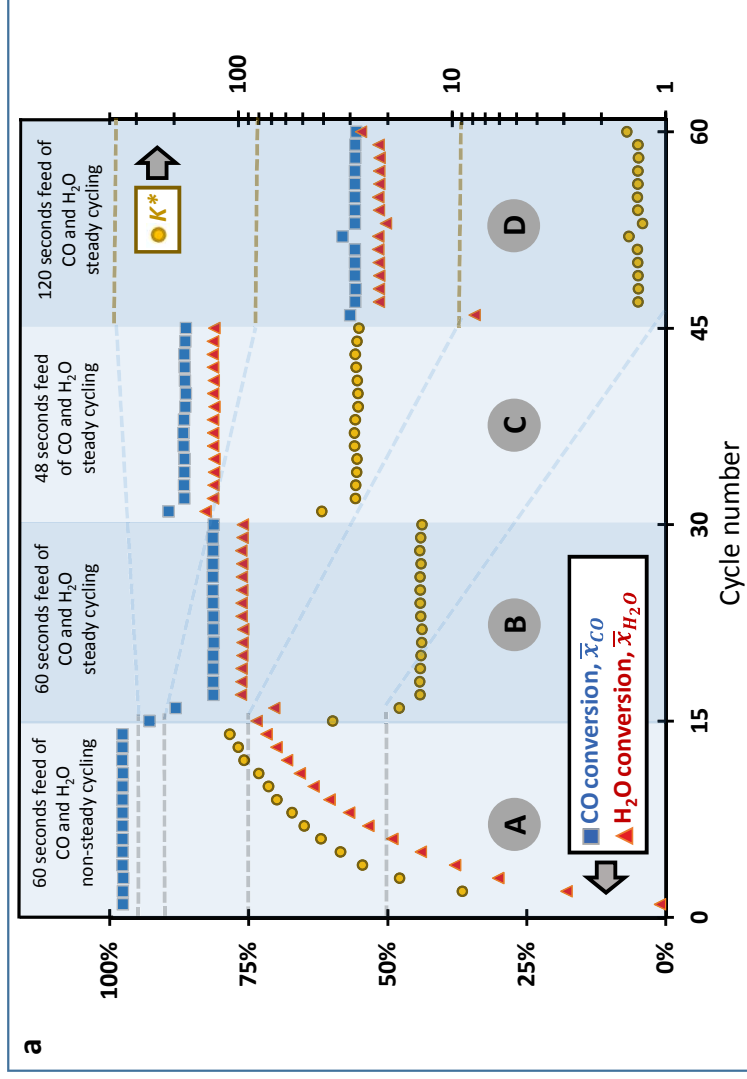
419 **Fig. 2. Conversion, reactor performance measure ( $K^*$ ) and outlet mole fractions (real**  
420 **and modelled) versus cycle number show that equilibrium limitations have been**  
421 **overcome. (a)** Time-averaged conversions of CO ( $\bar{x}_{CO}$ , squares) and H<sub>2</sub>O ( $\bar{x}_{H_2O}$ , triangles)  
422 on the left axis and reactor performance measure,  $K^*$ , on the right axis, as a function of cycle  
423 number for a reverse-flow memory reactor containing non-stoichiometric La<sub>0.6</sub>Sr<sub>0.4</sub>FeO<sub>3- $\delta$</sub> .  
424 Region A (evolution of the oxidation state profile) (Cycles 1-15) with 60-second feeds of CO  
425 and H<sub>2</sub>O, Region B (Cycles 16-30) with 60-second feeds, Region C (Cycles 31-45) with 48-  
426 second feeds, and Region D (Cycles 46-60) with 120-second feeds. The dashed lines are  
427 equivalence lines between an overall conversion and the corresponding measure of reactor  
428 performance. Note, that the  $K^*$  for Cycle 46 is 0.7 and is off-scale. The small difference  
429 between the conversions of CO and H<sub>2</sub>O are due to small differences in the flowrates  
430 between oxidising and reducing half cycles; the oxygen balance closes to within 97%. **(b),**  
431 **(c)** and **(d)** Measured effluent gas mole fractions versus time for representative cycles. **(e),**  
432 **(f)** and **(g)** Corresponding modelled effluent gas mole fractions versus time.

433

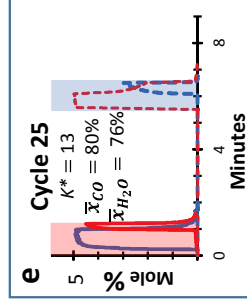
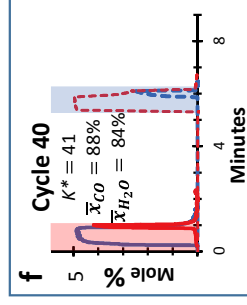
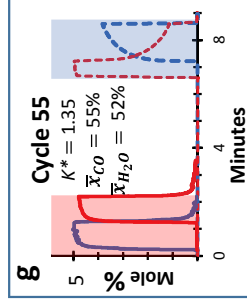
434 **Fig. 3. Representative shifts in  $2\theta$  peak positions and local oxygen content of the**  
435 **La<sub>0.6</sub>Sr<sub>0.4</sub>FeO<sub>3- $\delta$</sub>  versus reactor position showing changes in lattice parameter and**  
436 **oxygen content are a function of axial position. (a)** *Operando* XRD scans, arbitrary  
437 intensity, from the H<sub>2</sub>O-feed end of the reactor bed after the CO feed of Cycle 22 (red  
438 triangles) and the H<sub>2</sub>O feed of Cycle 23 (blue squares) showing the lower  $2\theta$  peak positions  
439 and thus larger cubic lattice parameter after CO feed compared to H<sub>2</sub>O feed. **(b)** Local  
440 oxygen content of the non-stoichiometric solid (La<sub>0.6</sub>Sr<sub>0.4</sub>FeO<sub>3- $\delta$</sub> ),  $3-\delta$ , relative to the local  
441 oxygen content of the reactor bed in the absence of chemical reaction,  $3-\delta^*$ , versus reactor  
442 position, for Region B in Fig. 2, immediately after oxidation (red triangles) and reduction  
443 (blue squares). The CO-feed end of the reactor remained the most reduced location (lowest  
444 oxygen content) and the H<sub>2</sub>O-feed end of the reactor the most oxidised (highest oxygen  
445 content). There is a profile in oxygen content which, although shifted, from oxidation to  
446 reduction, retains a memory of the gas feeds.







Experiment



Model

